Published in final edited form as:
*Magn Reson Med*. 2018 May ; 79(5): 2766–2772. doi:10.1002/mrm.26924.

# A comparison of exogenous and endogenous CEST MRI methods for evaluating *in vivo* pH

**Leila R. Lindeman**[1], **Edward A. Randtke**[2], **Rachel A. High**[1], **Kyle M. Jones**[3], **Christine M. Howison**[2], and **Mark D. Pagel**[1,2,3]

[1]Cancer Biology Graduate Interdisciplinary Program, University of Arizona Cancer Center, Tucson, AZ, USA

[2]Department of Medical Imaging, University of Arizona, Tucson, AZ, USA

[3]Department of Biomedical Engineering, University of Arizona, Tucson, AZ, USA

## Abstract

**Purpose—**Extracellular pH (pHe) is an important biomarker for cancer cell metabolism. AcidoCEST MRI uses the contrast agent iopamidol to create spatial maps of pHe. Measurements of amide proton transfer exchange rates ($k_{ex}$) from endogenous CEST MRI were compared to pHe measurements by exogenous acidoCEST MRI to determine whether endogenous $k_{ex}$ could be used as a proxy for pHe measurements.

**Methods—**Spatial maps of pHe and $k_{ex}$ were obtained using exogenous acidoCEST MRI and an endogenous CEST MRI analyzed with the Omega Plot method, respectively, to evaluate mouse kidney, a flank tumor model, and a spontaneous lung tumor model. The pHe and $k_{ex}$ results were evaluated using pixelwise comparisons.

**Results—**The $k_{ex}$ values obtained from endogenous CEST measurements did not correlate with the pHe results from exogenous CEST measurements. The $k_{ex}$ measurements were limited to fewer pixels and had a limited dynamic range relative to pHe measurements.

**Conclusion—**Measurements of $k_{ex}$ with endogenous CEST MRI cannot substitute for pHe measurements with acidoCEST MRI. While endogenous CEST MRI may still have good utility for evaluating some specific pathologies, exogenous acidoCEST MRI is more appropriate when evaluating pathologies based on pHe values.

## INTRODUCTION

Solid tumors generate and export excess lactic acid due to altered metabolism, dominated by glycolytic processes, resulting in acidic extracellular pH (pHe) in the tumor microenvironment (1). Lactic acid can also accumulate in the tumor microenvironment of highly angiogenic tumors due to poor perfusion (2). The quantification of tissue pHe can be

---

Corresponding Author: Mark D. Pagel, Ph.D., MD Anderson Cancer Center, 3SCR4.3642, Unit 1907, 1881 East Road, Houston, TX 77054-1901, Tel: +1-713-205-8515, mdpagel@mdanderson.org.

SUPPORTING INFORMATION
Additional Supporting Information that includes Supporting Table S1 may be found in the online version of this article.

a useful diagnostic tool for distinguishing between cancers and non-malignant pathologies (3,4). Furthermore, tumor pHe may be an important indicator of tumor metabolism, providing a useful biomarker for monitoring therapy response (5,6). While the intracellular compartment remains buffered in most living cells, intracellular pH (pHi) has also become a biomarker of interest is some pathologies. Intracellular acidification can occur in cases of extreme cell stress, in response to some chemotherapies, or ischemic stroke (7,8).

Chemical exchange saturation transfer (CEST) MRI can generate image contrast based on the exchange rate of a proton from an exogenous agent to water (9). The exchange rates of some labile protons are pH-dependent, causing CEST image contrast to be dependent on tissue pH. AcidoCEST MRI is a specific protocol that measures two CEST signals from an exogenous contrast agent to accurately and precisely measure tumor pHe *in vivo* (10). This method has been extensively refined, validated, and applied to study tumor models that have different pHe values, and to study effects of drugs that reduce metabolism (6). AcidoCEST MRI has also been translated to the clinic to measure tumor pHe in patients who have metastatic ovarian cancer (11).

The chemical exchange of amide protons from endogenous proteins can also generate CEST MR image contrast. The chemical exchange rate ($k_{ex}$) of amide protons with bulk water is base catalyzed in the physiological pH range, and therefore tumor acidosis should decrease CEST MRI contrast (12). Conversely, the concentration of endogenous amide protons increases CEST MRI contrast, especially from mobile proteins that have longer $T_1$ and $T_2$ relaxation time constants and are highly water-accessible (13). Therefore, endogenous CEST MRI of some solid tumors have shown no significantly different CEST contrast relative to normal tissues, presumably due to the opposed effects of tumor acidosis and mobile protein content in tumors (14). For these reasons, endogenous CEST results may be interpreted as a weighted average of pH and mobile protein concentrations.

To address this problem, $k_{ex}$ has been estimated from CEST MRI with multiple saturation powers using a variety of analysis methods (15–18). While the absolute amplitude of the CEST signal is dependent on the concentration of the exchangeable protons, this concentration does not affect the relative change in CEST with increasing saturation power. The QUantifying Exchange with Saturation Power (QUESP) method can estimate $k_{ex}$ in a concentration-independent manner by fitting a non-linear function to the CEST signal amplitudes measured with a range of saturation powers (15). The Omega Plot method, also known as the LB-QUESP method, is a linear version of the QUESP algorithm that can estimate $k_{ex}$ without requiring accurate initial guesses of the parameters (19).

We sought to compare exogenous and endogenous CEST MRI for *in vivo* pHe assessments. In particular, we aimed to determine whether endogenous $k_{ex}$ measurements could be used as a proxy for pHe measurements obtained with exogenous agents. We used acidoCEST MRI using an exogenous CEST agent to measure tumor pHe, and used the Omega Plot method to analyze endogenous CEST MRI results and directly measure endogenous $k_{ex}$. We performed these imaging assessments for the normal murine kidney, a spontaneous murine lung tumor model, and a flank xenograft mouse model of pancreatic cancer. The mouse kidney was studied to provide tissue with a variation in pHe and pHi; the flank tumor model was selected to test a model that is typically used in preclinical cancer research; the lung cancer model was evaluated to test conditions with higher image noise.

# METHODS

## Mouse models

MR imaging of normal kidneys was performed with female nude mice that were 12 weeks of age and 27 g average weight. To prepare a xenograft tumor model, $1X10^7$ MIA PaCa-2 pancreatic tumor cells in 100 μL of saline were injected subcutaneously in the right rear flank of male severe compromised immunodeficiency (SCID) mice, 8 weeks of age, 22.6 g average body weight. The flank tumor model grew to an average size of 200 $mm^3$ after 7 days, when they underwent MR imaging. To prepare an orthotopic model of lung adenocarcinoma, male A/J mice were treated with a single i.p. injection of 1 mg/g urethane in 0.2 mL PBS at 6 weeks of age. The lung adenocarcinomas reached a size of 1 mm at 25–26 weeks of age with average body weight of 29.4 g, which was suitable for MRI studies.

Prior to imaging, we anesthetized each mouse with 1.5 – 2.5% isofluorane in 1 L/min oxygen carrier gas. A tail vein was catheterized with a 27 g needle to deliver contrast agent. We used a fiber optic rectal probe to monitor temperature, and a respiration pad to monitor respiration rate (SA Instruments, Inc., Stony Brook, NY). To facilitate optimal respiratory gating, anesthesia levels were maintained such that mice had a respiratory rate of 20 – 50 breaths per minute. Mouse body temperature was maintained at 36.5–37.5 °C using warm air.

## MRI acquisitions

We performed anatomical MRI scans with each mouse to locate the kidney or tumor, using parameters listed in Table S1. We used a 7 T Bruker Biospec MRI scanner with a 20 cm bore and a 72 mm tranceiver volume coil (Bruker Biospin, Inc., Bilarica, MA). Respiration-gated acidoCEST MRI was performed by applying selective saturation at 3.5 μT power, followed by a Fast Imaging with Steady-state Precession (FISP) acquisition (all parameters are listed in Table S1) (20). For acidoCEST MRI of kidney and lung tumor model, we acquired images to produce four CEST spectra for each image pixel prior to i.v. administration of the contrast agent. Then 200 μL of 370 mg of iodine per ml (mgI/ml; 976 mM) of iopamidol (Isovue®, Bracco Diagnostics, Inc.) was injected i.v. within 60 sec, and the injection line was connected to a syringe pump that infused 400 μL/hour of agent during the next 30 minutes. This dose is equal to 5.66 – 7.36 gI/kg of mouse body weight. Because pharmacokinetics scale between species when normalized to body surface area, the dose used in our study equates to Human Equivalent Dose of 0.46 – 0.59 gI/kg. This dose is 2.5- to 3.3-fold lower than the maximum 1.5 gI/kg allowed for clinical CT (10,21,22). Six sets of CEST MR images were acquired immediately after injection to produce six post-injection CEST spectra for each imaging pixel (23). We used the same protocol for imaging the flank tumor model, except that we acquired 3 pre-injection and 5 post-injection CEST spectra because images of the flank tumor were less susceptible to motion artifacts.

For respiration-gated acidoCEST MRI, we achieved steady-state saturation by applying 10 rectangular-shaped pulses for 600 ms each (a total of 6 s). After this pulse train, the protocol checked the respiration trigger. If the trigger was active, then MR signal collection would commence (24). If the trigger was not active, another 600 ms saturation pulse would be delivered, and the protocol again checked for an active trigger to start MR signal collection, or delivered yet another 600 ms saturation pulse. This process was repeated until the protocol detected an active trigger and acquired the MR signal to produce an image.

Endogenous CEST images were acquired with selective saturation with rectangular-shaped pulses applied at 2.5, 3.5 and 4.5 ppm (Table S1). We collected images at 1.0, 1.5, and 2.0 μT saturation powers to calculate the amide $k_{ex}$. Large $B_0$ inhomogeneity in the lung due to air-tissue interfaces necessitated correction of the presaturation offsets. We used the offset value of the lung tumor ROI determined from the WASSR scan to correct the transmitter offset for the subsequent scans (25). This process greatly compensated for $B_0$ inhomogeneity in the lung tumor, and the post-processing method could then tolerate any remaining mild-to-moderate $B_0$ inhomogeneity on a pixelwise basis in the image of the lung tumor. The $B_0$ inhomogeneity was relatively small for imaging the kidney and xenograft tumor model, so that a similar WASSR scan to correct for large $B_0$ inhomogeneity was not required.

## MRI Analyses

AcidoCEST MRI results were fit using previously published methods (11, 23, 24, 26 – 28). We first averaged the four pre-injection images at each saturation frequency. We then applied a Gaussian spatial smoothing algorithm to improve signal-to-noise (23). We performed the same steps to process the six post-injection images. The resulting pre-injection image was subtracted from the post-injection image at each saturation frequency, which eliminated CEST signals from static endogenous sources. Pixels with contrast less than $2\sqrt{2}$(scan noise) we discarded from the analysis, because contrast above this threshold has a 95% probability of arising from the agent (26). CEST spectra were then obtained for each imaging pixel. A sum of three Lorentzian line shapes was fit to each CEST spectrum by varying the width, amplitude, and center frequency of each line shape (27). The CEST effects from iopamidol occur at 4.2 and 5.6 ppm, and the center peak for water was also fit. Each CEST spectrum was also fit with the Bloch-McConnell equations (the Bloch equations that include chemical exchange) modified to directly include pH as a fitting parameter, as previously described (28). We refer to this analysis method as Bloch fitting. Pixels with pHe values beyond the range of 6.2 – 7.4 pH units were excluded, based on an analysis of reliability previously evaluated with phantoms (23,28).

The contrast from endogenous CEST MRI at the various saturation powers was used to determine $k_{ex}$. The endogenous % CEST value was determined from MR image signals acquired with saturation at 2.5 ppm, 3.5 ppm and 4.5 ppm (Eq. [1]) (29). This analysis resulted in a measurement of CEST that is insensitive to MT and direct water saturation. We then used the % CEST values at different saturation powers to estimate the chemical exchange rate using the Omega Plot method, also known as LB-QUESP (Eq. [2]) (19). Although the linear HW-QUESP method can measure fast exchange rates with greater accuracy than the Omega Plot (30), amide protons from endogenous proteins have a slow chemical exchange rate of ~30 Hz, which justifies the use of the Omega Plot method (31).

$$\%CEST=\frac{\frac{(M_{sat}(+2.5)+M_{sat}(+4.5))}{2}-M_{sat}(+3.5)}{\frac{(M_{sat}(+2.5)+M_{sat}(+4.5))}{2}} \quad [1]$$

$$\frac{1}{\%CEST}-1=\frac{111}{c}k_{ex}R_1\left(\frac{1}{k_{ex}^2}+\frac{1}{\omega^2}\right) \quad [2]$$

where $M_{sat}$ is the MR image signal with saturation; $c$ is the concentration of the exchangeable protons on the agent in units of Molar; $k_{ex}$ is the chemical exchange rate in Hz; $R_1$ is the longitudinal relaxation rate in Hz; and $\omega$ is the saturation power in Hz. The factor of 111 represents the concentration of exchangeable protons on water, in units of Molar. The x-intercept of Equation [2] is equal to $-\frac{1}{k_{ex}^2}$.

# RESULTS

## MRI protocols

To facilitate the comparison of endogenous CEST MRI and acidoCEST MRI results, we performed both imaging protocols during the same imaging session for each mouse. Though the combination of respiration-gated endogenous CEST MRI and acidoCEST MRI protocols resulted in lengthy scan times, we successfully completed data collection without mouse fatality. Our respiration-gated acidoCEST MRI method performed well in all three murine models, as evidenced by the lack of motion artifacts in the images, including the images of lung tumors.

Lorentzian line shape fitting had potential to estimate pHe values from CEST spectra that had no CEST signal, rather than reporting that no pHe value could be reliably estimated. This problem was especially evident in CEST spectra from lung images that had greater noise than images of kidneys and flank tumors, where Lorentzian fitting was prone to fitting noise and estimated pHe values for many pixels in the empty space outside the mouse (Fig. 1c). Moreover, Lorentzian fitting estimated a wide range of pHe values within the physiological range of 6.2–7.4, making it difficult to determine whether the pHe values assigned in the ROI were accurate or precise. These results were consistent with a previous study of the accuracy and precision of the Lorentzian fitting method (11). For comparison, Bloch fitting had much less potential to report a reliable fit of CEST spectra that had no CEST signal. This fitting method estimated pHe values for many pixels throughout the lung tumor and surrounding lung tissue, and estimated pHe values in very few air regions in the lung or outside the mouse (Fig. 1b). When Bloch fitting encountered CEST spectra that were too noisy to fit reliably, this method estimated pHe values outside the physiological pHe range of 6.2–7.4, so that these pHe values could easily be discarded. This result was also consistent with a previous study of the Bloch fitting method (11).

### MRI results

The pHe values estimated with acidoCEST MRI were consistent with expectations in each model system (Figs. 2,3). The pHe values in the kidney were the most acidic (6.3 – 7.0), followed by the pHe values of the MiaPaCa flank xenograft (6.7–7.2), and the pHe values of the murine lung adenocarcinoma (6.9–7.4). More specifically, the slower growth of the lung tumors suggested slower metabolism for these tumors, which should produce less lactic acid and therefore have a higher pHe.

Our endogenous CEST MRI method measured proton exchange rates in fewer pixels relative to the acidoCEST method (Fig. 3c). More importantly, the chemical exchange rates quantified by endogenous CEST MRI did not correlate with the pHe values measured with acidoCEST MRI for all tissue types (Fig. 4). In addition, the dynamic range of the chemical exchange rates was narrow relative to the dynamic range of pHe values. While the pHe values spanned the entire measured pH range, with an approximately normal distribution (Fig. 5a), 80% of the $k_{ex}$ values were measured between 0 to 480 Hz of the 0–1200 Hz range (Fig. 5b). This result suggests that pHe measurements have a more direct interpretation with a dynamic range that has more value, while $k_{ex}$ measurements should be interpreted more carefully.

The uptake of iopamidol reached an average 35–49 mM concentrations in the kidney, flank tumor, and lung tumor, as estimated from Bloch fitting that included concentration as a fitting variable (Fig. 6a). The concentration of iopamidol varied within each tissue, ranging from a minimum of 0.1 μM to the maximum value of 100 mM allowed during fitting. The concentration of iopamidol was not correlated with pHe values in kidney and lung tumor (Fig. 6b–d). A slight negative correlation ($R^2 = 0.23$) was observed between concentration and pHe in the MIA PaCa-2 flank xenografts, wherein pixels with lower pHe values of 6.6 to 6.9 tended to show the highest concentration.

## DISCUSSION

The pHe values quantified by acidoCEST MRI were consistent with pHe values of other *in vivo* CEST MRI studies with exogenous agents. A previous *in vivo* pH imaging study that used a $T_1$ MRI contrast agent to measure renal pH in mice found that pH in the kidney ranged from 6.3 – 7.3 and also observed that the pH of the renal cortex was consistently higher than that of the medulla (32). The higher pHe observed in the slower-growing lung adenocarcinoma model relative to the faster growing xenograft pancreatic tumor model is consistent with prior studies examining tumor pHe and invasive phenotypes (33,34). The correlation between acidic pHe and increased production of VEGF that increases angiogenesis may explain the slight correlation between higher acidosis and higher uptake of iopamidol in the MIA PaCa-2 flank xenografts (35).

Overall, we observed no correlation between endogenous amide exchange rate measured with the Omega Plot method and pHe values measured with acidoCEST MRI. As a possible rationale, methods that measure the CEST effect from endogenous proteins are unable to distinguish between pHe and pHi that remains well buffered or partially buffered in living tumor cells (3). The influence of the buffered intracellular space on endogenous CEST MRI may be sufficient to explain the lack of dynamic range of $k_{ex}$ values observed in our endogenous CEST MRI results. Furthermore, the contrast used for endogenous CEST MRI analysis was lower than the CEST contrast generated by the exogenous contrast agent. This reduced sensitivity resulted in a reduced number of pixels that could be reliably analyzed by the Omega Plot method vs. acidoCEST MRI. For comparison, well-controlled CEST MRI studies with agarose phantoms of creatine have showed a correlation between CEST signal and pH (36), and also between CEST and concentration (37). Our results indicate that studies with homogenous phantoms may need to be carefully compared to more heterogenous in vivo conditions.

Our endogenous CEST MRI method allowed for direct quantitative comparison between pHe and amide proton CEST MRI. In particular, our multi-power Omega Plot analysis was designed to remove the effects of mobile protein concentration when evaluating $k_{ex}$, while $MTR_{asym}$ ratios include the effect of mobile protein content. As an alternative, a similar analysis method known as HW-QUESP also removes effects of $B_1$ inhomogeneity from the estimate of $k_{ex}$, although HW-QUESP underestimates slow $k_{ex}$ values (30). AREX, qCEST, and the combination of AREX and qCEST are other methods that improve the assessment of tissue pH using endogenous CEST MR images (17,18,38). However, neither approach addresses whether the source of the pH-dependent CEST contrast is intra- or extra-cellular. Extreme oxygen deprivation, as in ischemic stroke, may cause sufficient cellular trauma to result in un-buffered intracellular pH, but such extreme conditions are unlikely to be present in most tumors. The qCEST method (17,18) has the advantage of measuring concentration in addition to exchange rate of the labile pool. We were interested in whether exchange rate would correlate with pHe, and chose to use the simpler Omega Plot method as fewer parameters are needed to fit to experimental data. For future studies, the qCEST method could be used to determine whether concentration of endogenous proteins that generate CEST can correlate with pHe.

Other endogenous CEST MRI methods have been developed to measure additional sources of chemical exchange, such as CEST from amine and hydroxyl groups. Amine/amide concentration independent detection (AACID) can quantify tissue pH with very high precision (standard deviations as low as 0.05 pH units) (39). AACID studies have detected intracellular acidification resulting from treatment by a carbonic anhydrase inhibitor and the lactate transporter inhibitor lonidamine (40,41). A modified qCEST approach has been used to measure the pH of intervertebral discs in a porcine model by measuring the exchange of hydroxyl groups on glycosaminoglycan, showing that the proton exchange rate between that solute and water pools ($k_{sw}$) was linearly correlated with pH as measured by an electrode (42). However, just as with endogenous amide proton exchange analyzed using the Omega Plot method, endogenous amine and hydroxyl proton exchange are a weighted average of pHi and pHe, confounding the interpretation of AACID and qCEST. In addition, a pH electrode disrupts the structural integrity of the tissue, causing a weighted average of pHi and pHe to be measured. Compared to electrodes, acidoCEST MRI measures pHe with better selectivity and similar accuracy and precision (23,43). In that regard, exogenous acidoCEST MRI is an improved comparator for interrogating pHe. Overall, our study provides a foundation for future studies that compare CEST MRI methods that are sensitive to pH.

## CONCLUSION

We have provided evidence of a lack of correlation between pHe measurements with exogenous acidoCEST MRI and $k_{ex}$ measurements with endogenous multi-power CEST MRI analyzed with an Omega Plot. Our endogenous CEST MRI analysis was designed to provide a quantitative measure of $k_{ex}$ without influence from the endogenous mobile protein content in each pixel. Our endogenous CEST MRI method had lower contrast-to-noise than exogenous acidoCEST MRI, which resulted in the analysis of fewer pixels with endogenous CEST MRI. AcidoCEST MRI results showed a weak correlation between pHe and vascular uptake of the exogenous agent in a flank tumor model, suggesting some correlation between tumor acidosis and angiogenesis in this tumor type. Overall, our study reflected the advantages of acidoCEST MRI, while indicating that endogenous CEST MRI results during cancer studies should be carefully interpreted.

## Supplementary Material

Refer to Web version on PubMed Central for supplementary material.

## Acknowledgments

The authors would like to thank the Experimental Mouse Shared Resource of the University of Arizona for the development of the animal models used in this study. We would also like to thank George Munguia for his technical assistance. These studies were supported by NIH grants R01CA167183, P30CA023074, L.R.L was supported by 32CA009213, and K.M.J. was supported by T32HL007955 and T32HL066988.

## References

1. Warburg O. On the origin of cancer cells. Science. 1956; 123(3191):309–314. [PubMed: 13298683]
2. Sonveaux P, Copetti T, De Saedeleer CJ, Végran F, Verrax J, Kennedy KM, et al. Targeting the lactate transporter MCT1 in endothelial cells inhibits lactate-induced HIF-1 activation and tumor angiogenesis. PloS One. 2012; 7(3):e33418. [PubMed: 22428047]
3. Gillies RJ, Raghunand N, Garcia-Martin ML, Gatenby R. pH imaging. A review of pH measurement methods and applications in cancers. IEEE Eng Med Biol Mag. 2004; 23(5):57–64.
4. Wise HZ, Hung CY, Whiston E, Taylor JW, Cole GT. Extracellular ammonia at sites of pulmonary infection with Coccidioides posadasii contributes to severity of the respiratory disease. Microb Pathog. 2013; 59–60:19–28.
5. Parks SK, Chiche J, Pouyssegur J. pH control mechanisms of tumor survival and growth. J Cell Physiol. 2011; 226(2):299–308. [PubMed: 20857482]
6. Akhenblit PJ, Howison CM, Malm SW, Chen LQ, Baker AF, Pagel MD. Monitoring early therapeutic response by measuring extracellular pH in a tumor model with acidoCEST MRI. Cancer Res. 2014; 74(19 Supplement):LB-161.
7. Neri D, Supuran CT. Interfering with pH regulation in tumours as a therapeutic strategy. Nat Rev Drug Discov. 2011; 10(10):767–777. [PubMed: 21921921]
8. Siesjo BK. Pathophysiology and treatment of focal cerebral ischemia. Part I: Pathophysiology J Neurosurg. 2008; 108(3):616–631. [PubMed: 18312115]
9. Ward KM, Balaban RS. Determination of pH using water protons and chemical exchange dependent saturation transfer (CEST). Magn Reson Med. 2000; 44(5):799–802. [PubMed: 11064415]
10. Chen LQ, Howison CM, Jeffery JJ, Robey IF, Kuo PH, Pagel MD. Evaluations of extracellular pH within in vivo tumors using acidoCEST MRI. Magn Reson Med. 2014; 72(5):1408–1417. [PubMed: 24281951]

11. Jones KM, Randtke EA, Yoshimaru ES, Howison CM, Chalasani P, Klein RR, Chambers SK, Kuo PH, Pagel MD. Clinical translation of tumor acidosis measurements with acidoCEST MRI. Mol Imaging Biol. 2016; doi: 10.1007/s11307-016-1029-7
12. Englander SW, Downer NW, Teitelbaum H. Hydrogen exchange. Annu Rev Biochem. 1972; 41(1): 903–924. [PubMed: 4563445]
13. Yan K, Fu Z, Yang C, et al. Assessing amide proton transfer (APT) MRI contrast origins in 9 L gliosarcoma in the rat brain using proteomic analysis. Mol Imaging Biol. 2015; 17(4):479–487. [PubMed: 25622812]
14. Heo HY, Jones CK, Hua J, Yadav N, Agarwal S, Zhou J, van Zijl PCM, Pillai JJ. Whole-brain amide proton transfer (APT) and nuclear Overhauser enhancement (NOE) imaging in glioma patients using low-power steady-state pulsed chemical exchange saturation transfer (CEST) imaging at 7T: 7T APT and NOE imaging for glioma grading. J Magn Reson Imaging. 2016; 44(1):41–50. [PubMed: 26663561]
15. McMahon MT, Gilad AA, Zhou J, Sun PZ, Bulte JWM, van Zijl PCM. Quantifying exchange rates in chemical exchange saturation transfer agents using the saturation time and saturation power dependencies of the magnetization transfer effect on the magnetic resonance imaging signal (QUEST and QUESP): pH calibration for poly-L-lysine and a starburst dendrimer. Magn Res Med. 2006; 55(4):836–847.
16. Sun PZ. Simultaneous determination of labile proton concentration and exchange rate utilizing optimal RF power: radio frequency power (RFP) dependence of chemical exchange saturation transfer (CEST) MRI. J Magn Reson. 2010; 202(2):155–161. [PubMed: 19926319]
17. Sun PZ, Wang Y, Dai Z, Xiao G, Wu R. Quantitative chemical exchange saturation transfer (qCEST) MRI - RF spillover effect-corrected omega plot for simultaneous determination of labile proton fraction ratio and exchange rate. Contrast Media Mol Imaging. 2014; 9(4):269–275.
18. Wu R, Xiao G, Zhou IY, Ran C, Sun PZ. Quantitative chemical exchange saturation transfer (qCEST) MRI - omega plot analysis of RF-spillover-corrected inverse CEST ratio asymmetry for simultaneous determination of labile proton ratio and exchange rate. NMR Biomed. 2015; 28(3): 376–383. [PubMed: 25615718]
19. Dixon WT, Ren J, Lubag AJM, Ratnakar J, Vinogradov E, Hancu I, Lenkinski RE, Sherry AD. A concentration-independent method to measure exchange rates in PARACEST agents. Magn Reson Med. 2010; 63(3):625–632. [PubMed: 20187174]
20. Shah T, Lu L, Dell KM, Pagel MD, Griswold MA, Flask CA. CEST-FISP: A novel technique for rapid chemical exchange saturation transfer (CEST) MRI at 7T. Magn Reson Med. 2011; 65(2): 432–437. [PubMed: 20939092]
21. Guidance for Industry: estimating the maximum safe starting dose in initial clinical trials for therapeutics in adult healthy volunteers. U.S. Department of Health and Human Services Food and Drug Administration, Center for Drug Evaluation and Research (CDER); 2005.
22. Liu XD, Chen I. Prediction of drug clearance in humans from laboratory animals based on body surface area. Eur J Drug Metab Pharmacokinet. 2001; 26(4):249–256. [PubMed: 11808867]
23. Chen LQ, Randtke EA, Jones KM, Moon BF, Howison CM, Pagel MD. Evaluations of tumor acidosis within in vivo tumor models using parametric maps generated with acidoCEST MRI. Mol Imaging Biol. 2015; 17(4):488–496. [PubMed: 25622809]
24. Jones KM, Randtke EA, Howison CM, Pagel MD. Respiration gating and Bloch fitting improve pH measurements with acidoCEST MRI in an ovarian orthotopic tumor model. Proc SPIE Int Soc Opt Eng. 2016; 9788:978815.doi: 10.1117/12.2216418 [PubMed: 27212783]
25. Kim M, Gillen J, Landman BA, Zhou J, van Zijl PCM. Water saturation shift referencing (WASSR) for chemical exchange saturation transfer (CEST) experiments. Magn Reson Med. 2009; 61(6): 1441–1450. [PubMed: 19358232]
26. Liu G, Ali MM, Yoo B, Griswold MA, Tkach JA, Pagel MD. PARACEST MRI with improved temporal resolution. Magn Reson Med. 2009; 61(2):399–408. [PubMed: 19165903]
27. Hingorani DV, Montano LA, Randtke EA, Lee YS, Càrdenas-Rodríguez J, Pagel MD. A single diamagnetic catalyCEST MRI contrast agent that detects cathepsin B enzyme activity by using a ratio of two CEST signals. Contrast Media Mol Imaging. 2016; 11(2):130–138. [PubMed: 26633584]

28. Randtke EA, Granados JC, Howison CM, Pagel MD, Cárdenas-Rodríguez J. Multislice CEST MRI improves the spatial assessment of tumor pH. Magn Reson Med. 2016; doi: 10.1002/mrm.26348
29. Jin T, Wang P, Zong X, Kim SG. MR imaging of the amide-proton transfer effect and the pH-insensitive nuclear Overhauser effect at 9. 4 T. Magn Reson Med. 2013; 69(3):760–770. [PubMed: 22577042]
30. Randtke EA, Chen LQ, Corrales LR, Pagel MD. The Hanes-Woolf Linear QUESP method improves the measurements of fast chemical exchange rates with CEST MRI. Magn Reson Med. 2014; 71(4):1603–1612. [PubMed: 23780911]
31. Zhou J, Payen JF, Wilson DA, Traystman RJ, van Zijl PCM. Using the amide proton signals of intracellular proteins and peptides to detect pH effects in MRI. Nat Med. 2003; 9(8):1085–1090. [PubMed: 12872167]
32. Raghunand N, Howison C, Sherry AD, Zhang S, Gillies RJ. Renal and systemic pH imaging by contrast-enhanced MRI. Magn Reson Med. 2003; 49(2):249–257. [PubMed: 12541244]
33. Moellering RE, Black KC, Krishnamurty C, Baggett BK, Stafford P, Rain M, Gatenby RA, Gillies RJ. Acid treatment of melanoma cells selects for invasive phenotypes. Clin Exp Metastasis. 2008; 25(4):411–425. [PubMed: 18301995]
34. Estrella V, Chen T, Lloyd M, et al. Acidity generated by the tumor microenvironment drives local invasion. Cancer Res. 2013; 73(5):1524–1535. [PubMed: 23288510]
35. Xu L, Fukumura D, Jain RK. Acidic extracellular pH induces vascular endothelial growth factor (VEGF) in human glioblastoma cells via ERK1/2 MAPK signaling pathway: mechanism of low pH-induced VEGF. J Biol Chem. 2002; 277(13):11368–11374. [PubMed: 11741977]
36. Sun PZ, Benner T, Kumar A, Sorensen AG. An investigation of optimizing and translating pH-sensitive pulsed-chemical exchange saturation transfer (CEST) imaging to a 3 T clinical scanner. Magn Reson Med. 2008; 60(4):834–841. [PubMed: 18816867]
37. Dai Z, Ji J, Xiao G, Yan G, Li S, Zhang G, Lin Y, Shen Z, Wu R. Magnetization transfer prepared gradient echo MRI for CEST imaging. Plos One. 2014; 9(11):e112219. [PubMed: 25384020]
38. Zaiss M, Xu J, Goerke S, Khan IS, Singer RJ, Gore JC, Gochberg DF, Bachert P. Inverse $Z$-spectrum analysis for spillover-, MT-, and $T_1$-corrected steady-state pulsed CEST-MRI -- application to pH-weighted MRI of acute stroke. NMR Biomed. 2014; 27(3):240–252. [PubMed: 24395553]
39. McVicar N, Li AX, Goncalves DF, Bellyou M, Meakin SO, Prado MAM, Bartha R. Quantitative tissue pH measurement during cerebral ischemia using amine and amide concentration-independent detection (AACID) with MRI. J Cereb Blood Flow Metab. 2014; 34(4):690–698. [PubMed: 24496171]
40. Marathe K, McVicar N, Li A, Bellyou M, Meakin S, Bartha R. Topiramate induces acute intracellular acidification in glioblastoma. J Neurooncol. 2016; 130(3):465–472. [PubMed: 27613534]
41. McVicar N, Li AX, Meakin SO, Bartha R. Imaging chemical exchange saturation transfer (CEST) effects following tumor-selective acidification using ionidamine. NMR Biomed. 2015; 28(5):566–575. [PubMed: 25808190]
42. Zhou Z, Bez M, Tawackoli W, et al. Quantitative chemical exchange saturation transfer MRI of intervertebral disc in a porcine model. Magn Reson Med. 2016; 76(6):1677–1683. [PubMed: 27670140]
43. Moon BF, Jones KM, Chen LQ, Liu P, Randtke EA, Howison CM, Pagel MD. A comparison of iopromide and iopamidol, two acidoCEST MRI contrast media that measure tumor extracellular pH. Contrast Media Mol Imaging. 2015; 10(6):446–455. [PubMed: 26108564]

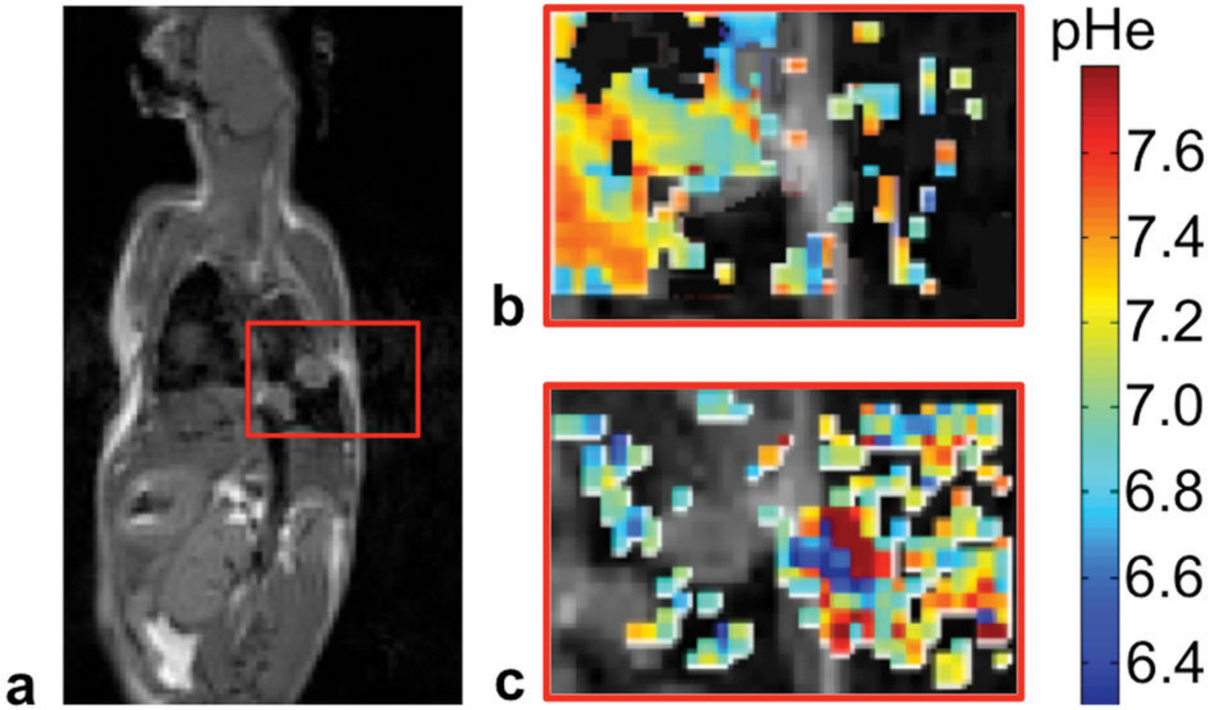

**FIGURE 1. Bloch-McConnell and Lorentzian line shape fitting methods for acidoCEST MRI**

a) The anatomical image shows the location of the lung tumor. The red box indicates the regions shown in panels b and c. Parametric maps of tissue pHe from acidoCEST MRI fit with b) the Bloch-McConnell equations modified to include pH as a fitting parameter, and c) Lorentzian line shape fitting show that Bloch fitting estimated pHe values primarily in tissue regions, while Lorentzian fitting estimated pHe values primarily in air regions.

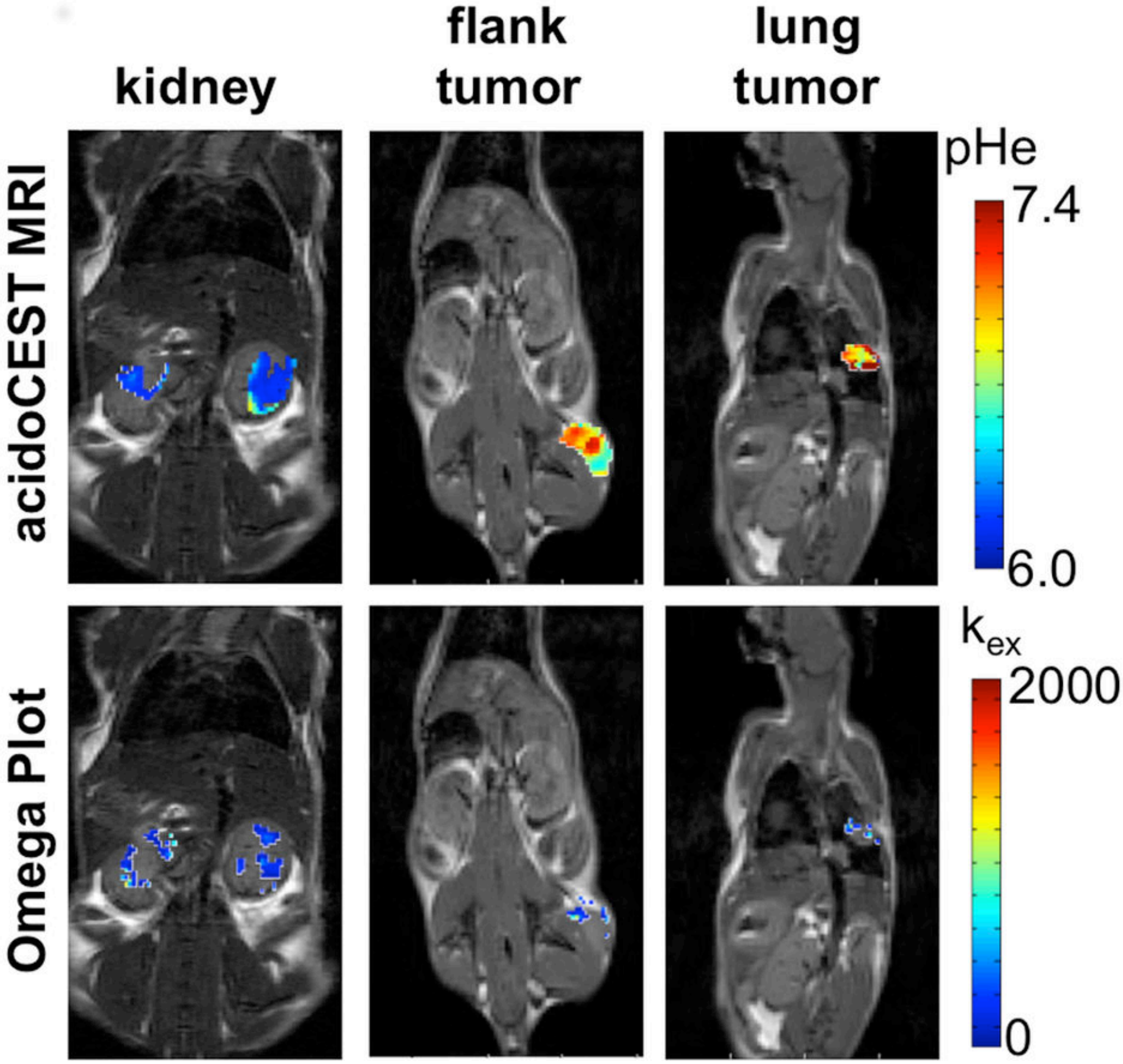

**FIGURE 2. AcidoCEST MRI and endogenous CEST MRI examples**

Representative parametric maps of pHe from acidoCEST MRI (top) and chemical exchange rate ($k_{ex}$) from endogenous CEST MRI (bottom) are overlaid on anatomical images.

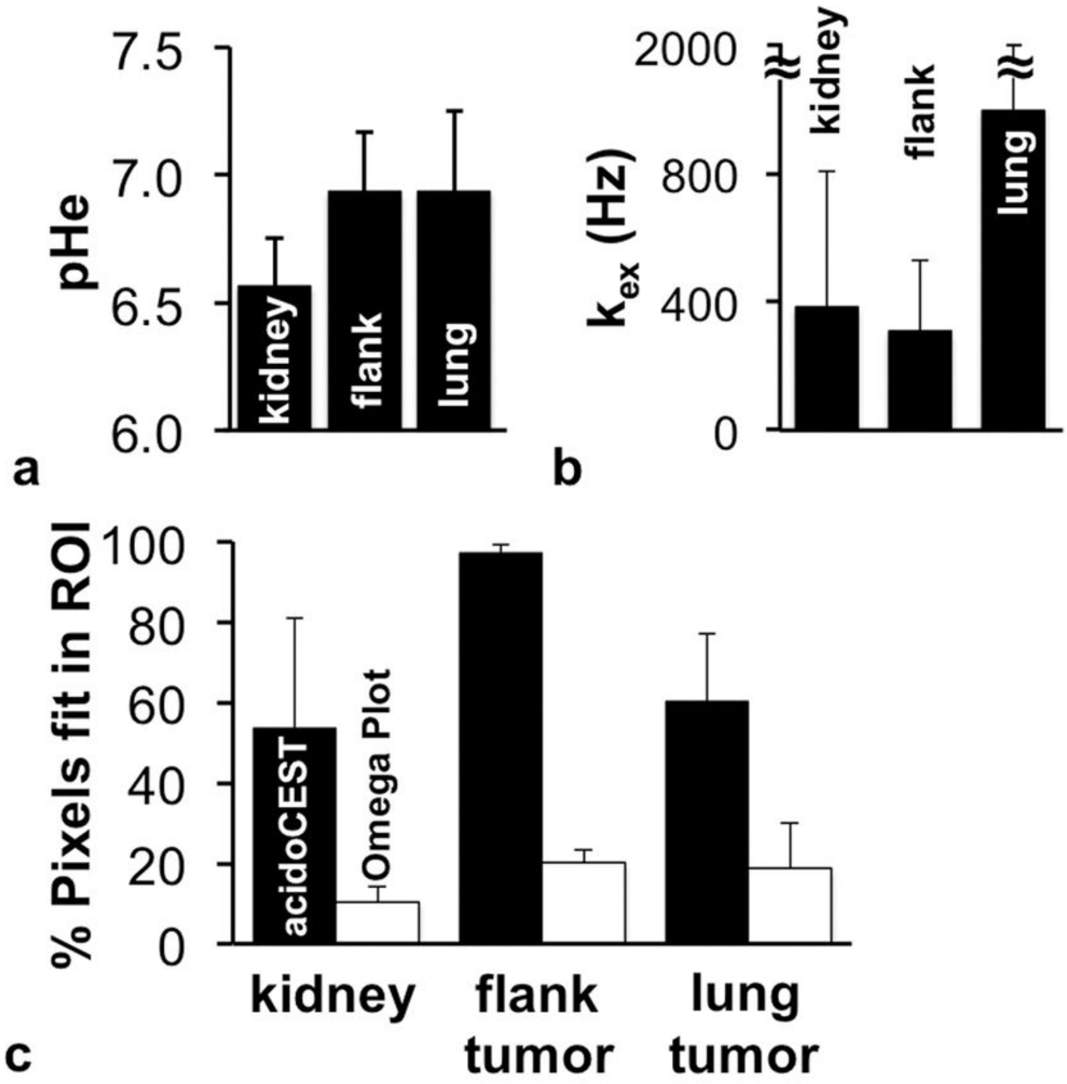

**FIGURE 3. AcidoCEST MRI and endogenous CEST MRI**

b) The average pHe of the kidney was lower than the average pHe of the flank tumor and lung tumor. c) The average $k_{ex}$ of the kidney and flank tumor were lower than the average $k_{ex}$ of the lung tumor. d) The $k_{ex}$ values could only be reliably fit for a fraction of the tissue regions, while pHe could be estimated for the majority of each tissue. Error bars represent the standard deviations of the distributions of pixels.

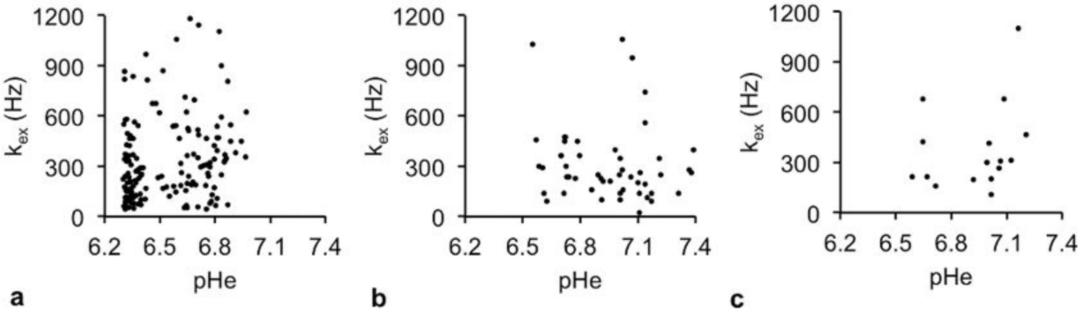

**FIGURE 4. Evaluations of the correlations between pHe and chemical exchange rate ($k_{ex}$)**

The a) kidney, b) flank xenograft tumor, and c) lung tumor showed no correlation between pHe and $k_{ex}$. pHe values were estimated from acidoCEST MRI using the Bloch-McConnell equations modified to include pH as a fitting parameter. The $k_{ex}$ values were estimated from endogenous CEST MRI with acquisitions at multiple saturation powers. $N = 3$ mice for each tissue type.

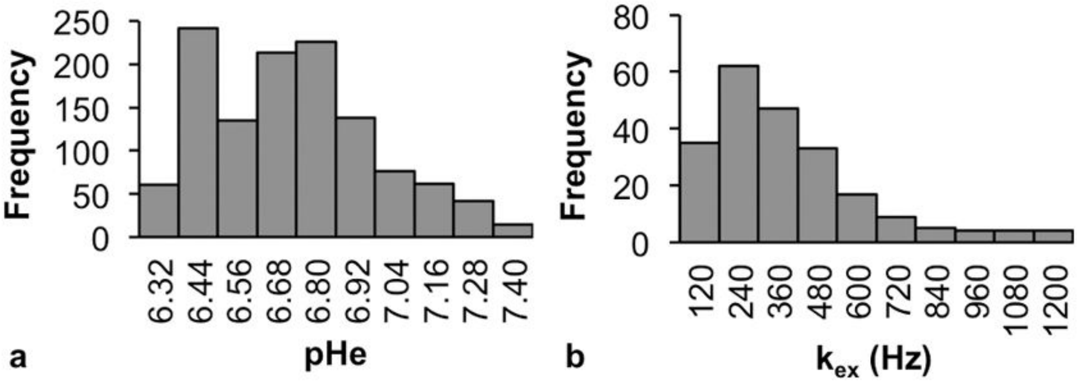

**FIGURE 5.**

Histograms showing the data distributions of (a) pHe and (b) $k_{ex}$ in all three tissue types combined. In (a) the range of possible pHe values (6.2 – 7.4) was divided into 10 equal bins. In (b), five outliers ( > 1400 Hz) were excluded, and the remaining $k_{ex}$ values, ranging from (0 – 1200 Hz) were divided into 10 equal bins.

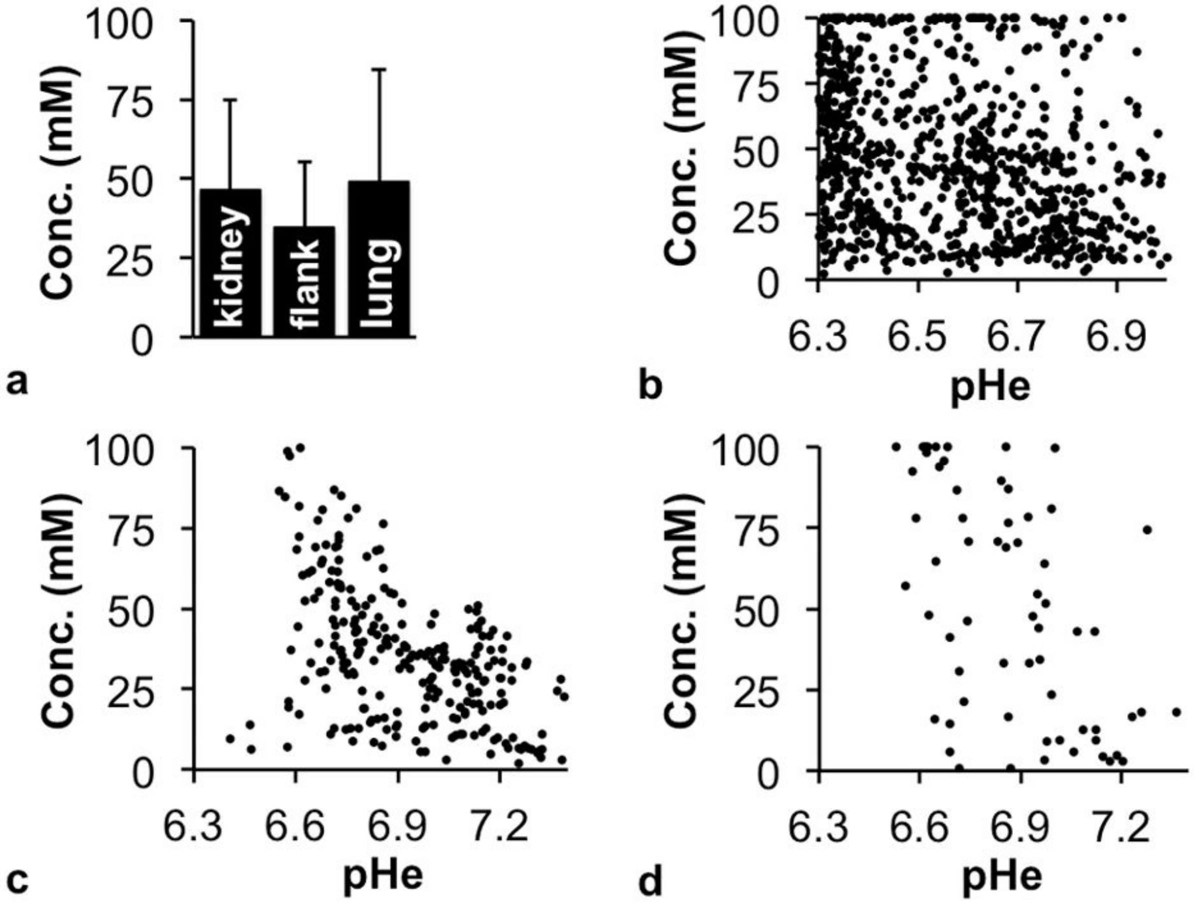

**FIGURE 6.**

The effect of agent concentration on pHe measurements with acidoCEST MRI. a) The average concentration of iopamidol in kidney, flank tumor and lung tumor estimated with Bloch fitting of pixelwise CEST spectra showed good uptake of agent in all three tissue types. Error bars represent the standard deviations of the distributions of pixels. The agent concentrations and pHe values were uncorrelated for b) kidney, c) flank xenograft tumor, and d) lung tumors on a pixelwise basis. Voxels where pHe data could not be fit were excluded. $N = 3$ mice for each tissue type.